Lightweight $Fe_{47}Mn_{25}Al_{13}Cr_7Ni_5C_3$ medium-entropy alloy with enhanced mechanical properties

Gang Hee Gu [a,1], Hyeonseok Kwon [a,1], Jae Heung Lee [a], Takayoshi Nakano [b], Hyoung Seop Kim [a,c,d,e,f,*]

[a] Department of Materials Science and Engineering, Pohang University of Science and Technology (POSTECH), Pohang, 37673, Republic of Korea
[b] Division of Materials and Manufacturing Science, Graduate School of Engineering Osaka University, Osaka, 565-0871, Japan
[c] Graduate Institute of Ferrous & Energy Materials Technology, Pohang University of Science and Technology (POSTECH), Pohang, 37673, Republic of Korea
[d] Center for Heterogenic Metal Additive Manufacturing, Pohang University of Science and Technology (POSTECH), Pohang, 37673, Republic of Korea
[e] Institute for Convergence Research and Education in Advanced Technology, Yonsei University, Seoul, 03722, Republic of Korea
[f] Advanced Institute for Materials Research (WPI-AIMR), Tohoku University, Sendai, 980-8577, Japan

ARTICLE INFO

ABSTRACT

In this study, we designed a lightweight $Fe_{47}Mn_{25}Al_{13}Cr_7Ni_5C_3$ medium-entropy alloy (MEA) (calculated density of 6.803 g/cm^3) with enhanced mechanical properties. The MEA samples were produced in three conditions with varying microstructures via thermomechanical processing. They achieved excellent tensile properties through strengthening mechanisms such as partial recrystallization, ultrafine grains, and $M_{23}C_6$ and B2 precipitates. Different strengthening mechanisms were applied depending on the annealing heat treatment conditions, resulting in three different strength-elongation combinations. Furthermore, the MEA, under all designed conditions, exhibited superior specific yield strength-uniform elongation and specific ultimate tensile strength-uniform elongation combinations compared to previously studied lightweight high-entropy alloys (HEAs) and lightweight steel. This was primarily attributed to the combination of benefits obtained from the low proportion of iron (47 at%) as a principal element and the large amount of aluminum addition (13 at%). The proposed MEA and its design strategy can satisfy the requirements for lightweight, cost-effective, strong, and ductile metallic materials, making a great contribution to the automotive industry in terms of crash resistance and fuel efficiency.

1. Introduction

Conventional alloy designs typically consist of a single principal element and small amounts of solute elements, but the materials' performance enhancement reached a bottleneck by the limited combination of elements [1,2]. Breaking with traditional wisdom, Cantor et al. [3] and Yeh et al. [4] proposed multi-principal element alloys (MPEAs) as a new alloy design concept in 2004. MPEAs are classified into high-entropy alloys (HEAs) and medium-entropy alloys (MEAs) based on the total configurationally molar entropy value in an ideal solid solution, and their significance lies in their ability to expand the elemental combinations limited by traditional alloy designs [5]. HEAs and MEAs, which classically had only single-phase solid solution microstructures with their high configuration entropy, have been designed over the past

few years to have excellent mechanical properties through various deformation mechanisms such as dislocation strengthening, deformation twinning, hetero deformation-induced strengthening [6,7], deformation-induced transformation strengthening [8–10], and precipitation strengthening [11,12].

Recently, as concerns for user safety and CO_2 reduction have increased, the automobile manufacturing industry has demanded strong, ductile, and lightweight metallic materials to simultaneously satisfy crash resistance and fuel efficiency. In accordance with these circumstances, HEAs/MEAs design strategies have also shifted toward developing lightweight alloys with low-density elements instead of alloys composed of heavy metal elements. For example, Liao et al. [13,14] designed low-density body-centered cubic (BCC) single-phase $Ti_x(-AlCrNb)_{100-x}$ MEAs using thermodynamic calculations and obtained

excellent mechanical properties with a compressive yield strength (YS) of over 1 GPa via thermomechanical processing. Wang et al. [15] designed a lightweight $Al_{17}Ni_{34}Ti_{17}V_{32}$ HEA with reasonable compressive properties at both room and high temperatures by precipitating low-density-elements-containing $L1_2$ phase in a BCC matrix.

In this study, we designed a lightweight MEA (calculated density of 6.803 g/cm^3) with a chemical composition of $Fe_{47}Mn_{25}Al_{13}Cr_7Ni_5C_3$ (in at%). The alloy composition of the MEA was based on Fe–Mn–Al–C steels, which are well known as lightweight steel [16,17]. The reason for designing the MEA by expanding the steel system was to have excellent mechanical properties and reasonable price competitiveness. In addition to the existing strategy of improving strength by adding carbon to induce precipitation of hard carbides, a small amount of nickel content brought additional strength improvement to the MEA through precipitation of the AlNi-rich B2 phase. The quite high aluminum (theoretical density of 2.710 g/cm^3) fraction of 13 at% contributed not only to the precipitation of the B2 phase but also to the low-density of the MEA. Reducing the iron (theoretical density of 7.874 g/cm^3) content and increasing the manganese (theoretical density of 7.260 g/cm^3) and chromium (theoretical density of 7.150 g/cm^3) contents also contributed to light-weighting the MEA. Furthermore, three different combinations of strength and elongation were obtained by controlling the microstructural evolution driving force through various annealing heat treatment temperatures. This research has the potential to yield valuable contributions to materials research, particularly in the development of a new lightweight MEA with tailored properties and cost competitiveness. These outcomes can have practical applications in various industries and advance our understanding of materials science principles.

2. Experimental procedures

2.1. Sample preparation

An ingot of the $Fe_{47}Mn_{25}Al_{13}Cr_7Ni_5C_3$ (in at%) MEA was cast into a graphite mold with a dimension of $7 \times 33 \times 80$ mm^3 using vacuum induction melting equipment (MC100V, Indutherm, Germany) under an argon atmosphere. Metal pellets of Fe, FeC, Mn, Al, Cr, and Ni with a purity of 99.9% or more were used as starting elements. The as-cast ingot was then homogenization heat treated at 1200 °C for 6 h in an argon atmosphere, followed by water quenching. It was subsequently cold-rolled at room temperature from a thickness of ~7.0 mm to ~1.2 mm (corresponding to an ~84% thickness reduction ratio). The as-rolled sheet was annealed at 700 °C, 800 °C, and 900 °C, each for 30 min under an argon atmosphere, followed by water quenching. These annealed samples are denoted as A700, A800, and A900, respectively, according to the annealing heat treatment temperatures.

2.2. Mechanical properties evaluations

The uniaxial tensile tests were conducted to evaluate the mechanical properties of the MEA. Before the tensile testing, the dog bone-shaped tensile specimens with a gauge length of 6.4 mm and a gauge width of 2.5 mm were cut from the MEA sheet using wire-cut electrical discharge machining. The tensile tests were then conducted by evaluating the load values using a universal testing machine (UTM; Instron 1361, Instron Corp., USA) and measuring the displacements using digital image correlation (DIC) equipment (ARAMIS M12, GOM Optical Measuring Techniques, Germany). The tensile stress-strain curves were calculated by combining the obtained load data and displacement data.

2.3. Microstructural analyses

The synchrotron X-ray diffraction (SXRD) experiments were performed to identify the constitutive phases of the MEA at the 8D beamline of Pohang Accelerator Laboratory (PAL). The 8D beamline used an X-ray

energy of 12.0 keV and a wavelength of 1.0258 Å. The SXRD experimental conditions were set to a step size of 0.02° and a holding time of 10 s for each step. Then, the typical microstructures of the MEA were observed using the backscatter electron (BSE) mode of field emission scanning electron microscopy (FE-SEM; JSM-7800F PRIME, JEOL Ltd., Japan). The transmission electron microscopy (TEM) analyses were performed using FE-TEM (JEM-2100F, JEOL Ltd., Japan) for further detailed microstructural characterization. Dual-beam focused ion beam (FIB; Helios Hikari UMSII, FEI, USA) with Ga$^+$ ion beam was employed for lift-out and sharpening preparation of the TEM specimens.

3. Results and discussion

3.1. Alloy design concept

Computational thermodynamics calculations were carried out to predict the outcome of our design strategy. The thermodynamics calculations were performed using Thermo-Calc software [18] with the TCFE2000 thermodynamic database and its upgraded version. Fig. 1 shows the thermodynamically calculated equilibrium phase fraction as a function of temperature for the designed MEA. As mentioned in the Introduction section, we sought to improve the mechanical properties by controlling the aluminum- and carbon-derived precipitates and the recrystallization driving force in terms of thermomechanical processing. The aluminum- or carbon-derived precipitates contribute to strength enhancement by precipitation strengthening based on the Orowan bypassing mechanism in grain interior and by composite strengthening based on the load transfer mechanism at grain boundaries [19,20]. In other words, as the fraction of the precipitates increases, strength improves at the expense of elongation. As the fraction of the recrystallized region increases from the severely deformed cold-rolled microstructure, the area where dislocation can be generated and accumulated increases, resulting in a reduction in strength and an improvement in elongation [21]. Considering these two aspects, we selected three post-cold-rolling annealing temperatures: 700 °C, 800 °C, and 900 °C.

The equilibrium phase diagram of the A700 sample exhibited co-precipitation of B2 and $M_{23}C_6$ phases in the face-centered cubic (FCC) matrix, and the relatively low annealing temperature of 700 °C may have resulted in a partially recrystallized microstructure. It is expected that the A700 sample will show a combination of high strength and low ductility among the presented process conditions. The constitute phases of the A800 sample are expected to be the same as those of the A700 sample, but it has a relatively sufficient recrystallization driving force with a higher annealing temperature. Hence, the fraction of the
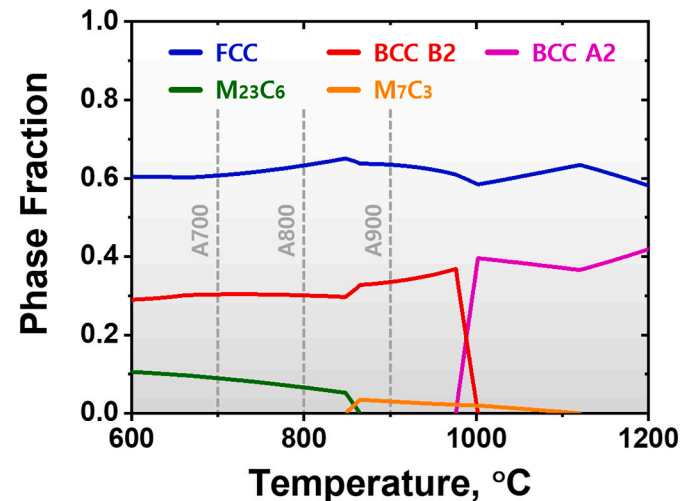

Fig. 1. Calculated mole fractions of equilibrium phases in the temperature range of 600 °C to 1200 °C for the $Fe_{47}Mn_{25}Al_{13}Cr_7Ni_5C_3$ MEA.

recrystallized region may have increased or may have been completely recrystallized to generate ultra-fine grains. In the A900 sample, it was calculated to have major precipitation of the B2 phase and minor precipitation of the M_7C_3 phase, rather than the $M_{23}C_6$ phase. Moreover, a temperature of 900 °C is expected to be sufficient to achieve a fully recrystallized microstructure.

3.2. Initial microstructure

High-resolution SXRD experiments were performed to detect minor phases as much as possible, and the SXRD patterns for the transverse direction (TD) plane of the A700, A800, and A900 samples are presented in Fig. 2. All MEAs under the performed annealing heat treatment conditions had the FCC phase matrix as the major peak, but the peak intensity of each orientation was somewhat different. Based on the wavelength used in the SXRD experiments (1.0258 Å), the peaks corresponding to the FCC matrix were $2\theta = \sim28.14°$, $\sim32.60°$, $\sim46.78°$, $\sim55.46°$, and $\sim58.18°$. These peaks correlate with (111), (200), (220), (311), and (222) planes, respectively. In the A700 sample, the peaks of the (111) and (220) planes were dominant, and other FCC peaks showed very low intensities. Such peak intensities concentrated on the (111) and (220) planes indicate that the A700 sample was not completely recrystallized and the texture generated by cold-rolling remains [22]. The FCC peaks of the A800 sample also exhibited stronger intensities on the (111) and (220) planes but were different from the A700 sample in that the intensities of the (200), (311), and (222) planes were improved. It indicates that the A800 sample also had a partially recrystallized microstructure and that recrystallization had progressed more than the A700 sample. Meanwhile, the A900 sample with sufficient recrystallization driving force showed SXRD peaks that were fully recrystallized without preferential orientation.

In addition to the texture of the FCC matrix, the formed precipitates were investigated using SXRD patterns. The A700 and A800 samples precipitated the same types of phases as the computational thermodynamics calculations in Fig. 1. In the A700 sample, peaks corresponding to the B2 and $M_{23}C_6$ phases were detected with very low intensities. The same peaks indicating the precipitates were also observed in the A800 sample. While the $M_{23}C_6$ phase peak intensities in the A800 sample were as low as in the A700 sample, the peaks of the B2 phase exhibited stronger intensities. That is, more B2 phase would have been precipitated in the A800 sample compared to the A700 sample. In contrast to the successful predictions for the A700 and A800 samples, the A900
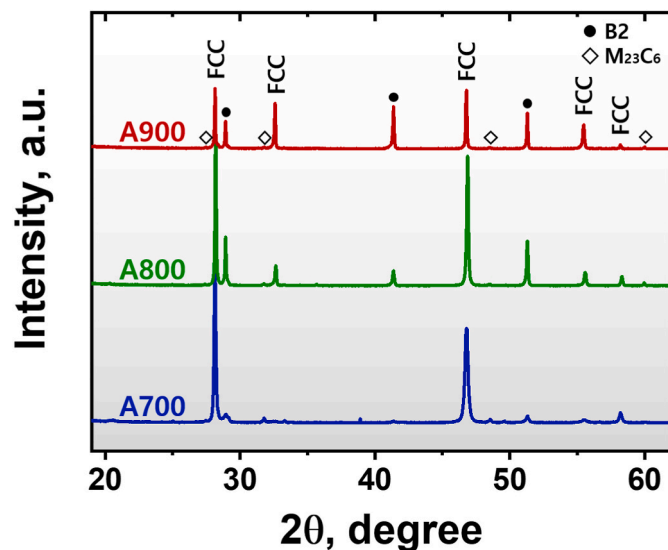
sample showed results that differed from the thermodynamic calculations. While it was predicted that the B2 and M_7C_3 phases were precipitated in the FCC matrix, the B2 and $M_{23}C_6$ peaks were detected in the A900 sample as in other samples. It is expected that the prediction error of the A900 sample is mainly due to the need to extrapolate from the existing databases to calculate the MEA that deviate from conventional alloy system [23]. Therefore, the designed MEA had FCC phase matrix and B2 and $M_{23}C_6$ precipitates under all performed heat treatment conditions.

The BSE micrographs for the performed heat treatment conditions are shown in Fig. 3 to provide direct microstructural observations. The low-magnification BSE image of the A700 sample exhibited coarse grains with a deformed structure elongated in the rolling direction (RD), which is a typical cold-rolled microstructure (Fig. 3(a1)) [24,25]. In the high-magnifications BSE images of the A700 sample, nanometer-sized grains were observed that recrystallized by heterogeneous nucleation along the rolling shear bands, which are oriented at 35°-40° with respect to the RD (Fig. 2(a2)-(a4)) [26]. Considering the SXRD patterns in Fig. 2, the recrystallized nanometer-sized grains contain the B2 and $M_{23}C_6$ phases as well as the FCC phase matrix. Although recrystallized nanometer-sized grains were present along the rolling shear bands, most regions showed a cold-rolled microstructure with unresolved dislocations. This indicates that it is difficult for the MEA to achieve significant microstructural evolution (i.e., recovery, recrystallization, and grain growth) under heat treatment conditions at 700 °C for 30 min.

The low-magnification BSE image distinguishes the microstructure of the A800 sample into the recrystallized regions and elongated prior grain regions (Fig. 3(b1)). Unlike the A700 sample, which consisted only of coarse grains with a deformed structure elongated along the RD, the A800 sample had some recrystallized regions with an equiaxed fine grain structure (Fig. 3(b2)). In the recrystallized region of the A800 sample, annealing twins generated during annealing heat treatment and randomly distributed precipitates regardless of grain interior and grain boundaries were observed (Fig. 3(b3)). Furthermore, the elongated prior grain regions of the A800 sample showed two types of specific microstructures. (i) With the relatively large microstructural evolution driving force compared to the A700 sample, the cold-rolled grains with unresolved dislocations inside the elongated prior grain regions were recovered by annihilation and rearrangement mechanisms and transformed into several small grains. (ii) Some prior grains remained as deformed structures and recrystallized nanometer-sized grains along with rolling shear bands, similar to the A700 sample.

The MEA was fully recrystallized under the annealing heat treatment condition of the A900 sample, and its ultrafine grains had annealing twins and precipitates identical to the microstructure of the recrystallized region of the A800 sample (Fig. 3(c)). What is interesting about the microstructure of the A900 sample is that it presented a bimodal grain size harmonic structure where relatively coarse grains are surrounded by relatively fine grains [27]. Accordingly, Fig. 3(c2) and 3(c3) show different grain sizes even though they are BSE micrographs of the same magnification. This is mainly due to differences in nucleation rates depending on the regions. The shear bands, which are heterogeneous nucleation sites, were recrystallized first, and the regions located between the shear bands were recrystallized next. The recrystallized grains subsequently undergo grain growth during annealing heat treatment, so the regions corresponding to the shear bands have relatively coarse grains and the regions between them have relatively fine grains, resulting in the formation of such harmonic structures.

The designed MEA was fully recrystallized only when the annealing heat treatment temperature was above 900 °C, which requires higher temperatures for microstructural evolution compared to other HEA and MEA systems. For example, the recrystallization onset temperature of the CoCrFeMnNi HEA was measured to be 600 °C, and the cold-rolled microstructure could be completely recrystallized by annealing heat treatment at 600 °C for 30 min [28,29]. The CoCrNi MEA exhibited a partially recrystallized microstructure when annealing heat treated at
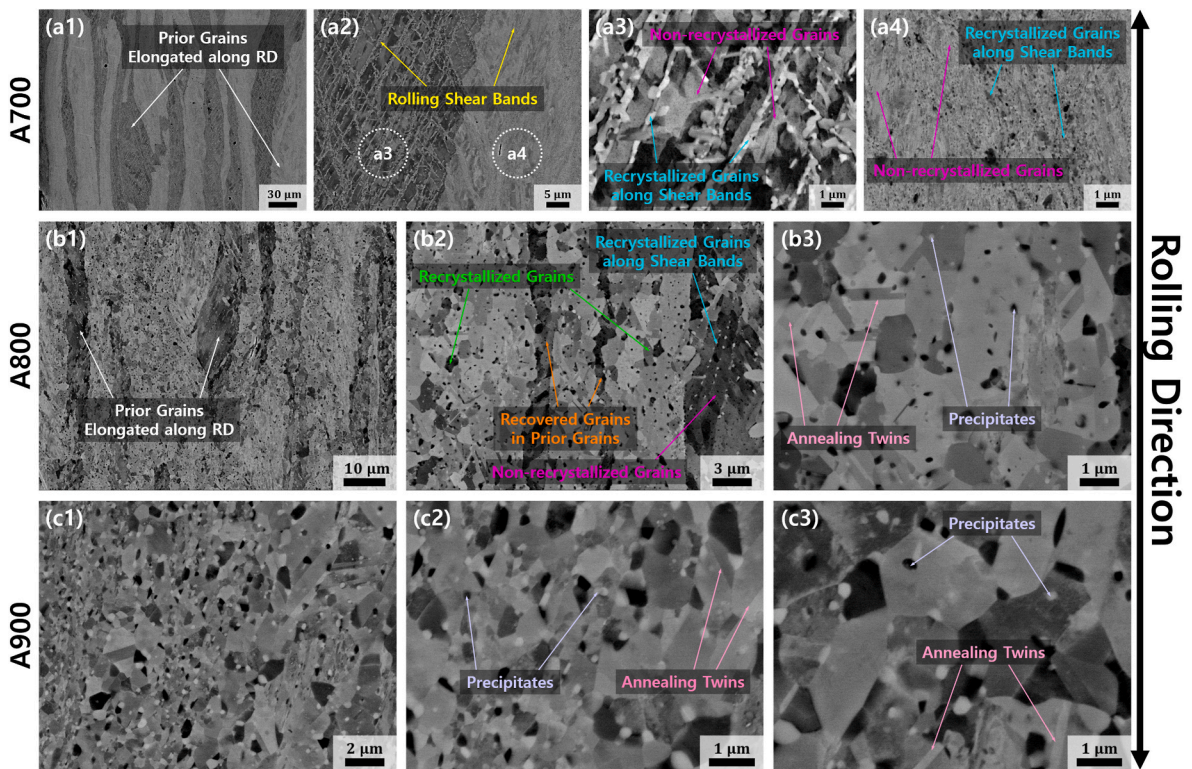

Fig. 2. SXRD patterns of the $Fe_{47}Mn_{25}Al_{13}Cr_7Ni_5C_3$ MEA subjected to A700, A800, and A900 annealing heat treatment.

Fig. 3. BSE micrographs at various magnifications for the **(a)** A700, **(b)** A800, and **(c)** A900 samples. White, yellow, magenta, cyan, light green, orange, light pink, and light purple arrows indicate prior grains elongated along RD, rolling shear bands, non-recrystallized grains, recrystallized grains along shear bands, recrystallized grains, recovered grains in prior grains, annealing twins, and precipitates, respectively. (For interpretation of the references to colour in this figure legend, the reader is referred to the Web version of this article.)

650 °C for 60 min, but was fully recrystallized when annealing heat treated at 700 °C for 60 min [30]. The slow kinetics of the MEA were mainly contributed by the addition of carbon, which is well-known to retard recrystallization [26,31]. As interstitial atoms, carbon solutes play a role in preventing recrystallization by blocking grain boundary movement through interaction between grain boundaries and solute atmosphere, leading to a partially recrystallized microstructure in the A700 and A800 samples. Furthermore, the addition of aluminum and carbon elements induces the precipitation of B2 and $M_{23}C_6$ phases, which causes sluggish grain growth kinetics by the Zener pinning effect and thus produces ultrafine grains in the A900 sample [32].

To investigate the microstructure in more detail, TEM experiments were performed on the A800 and A900 samples. The nanostructure of the A700 sample was not observed because it had an obvious deformed structure. Fig. 4 shows scanning TEM bright-field (STEM BF)

micrographs of recovered and recrystallized grains observed in the A800 and A900 samples. The grains recovered inside the prior grains of the A800 sample were composed of precipitates located at grain boundaries and a matrix in which dislocations were almost released (Fig. 4(a)). Only $M_{23}C_6$ precipitates were identified in the recovered grains of the A800 sample. In some recovered grains, arrayed dislocations undergoing rearrangement were observed as evidence of recovery. Meanwhile, the recrystallized region of the A800 sample and the fully recrystallized A900 sample showed similar microstructures (Fig. 4(b) and (c)). The precipitates were randomly distributed regardless of matrix and grain boundaries in the recrystallized regions, and the coexistence of Cr-rich $M_{23}C_6$ carbide and AlNi-rich B2 phase was confirmed through TEM-energy dispersive spectroscopy (EDS) elemental mapping results (Fig. 5). Such randomly distributed dual-precipitation acts as an obstacle to dislocations by the Orowan mechanism, resulting in reasonable
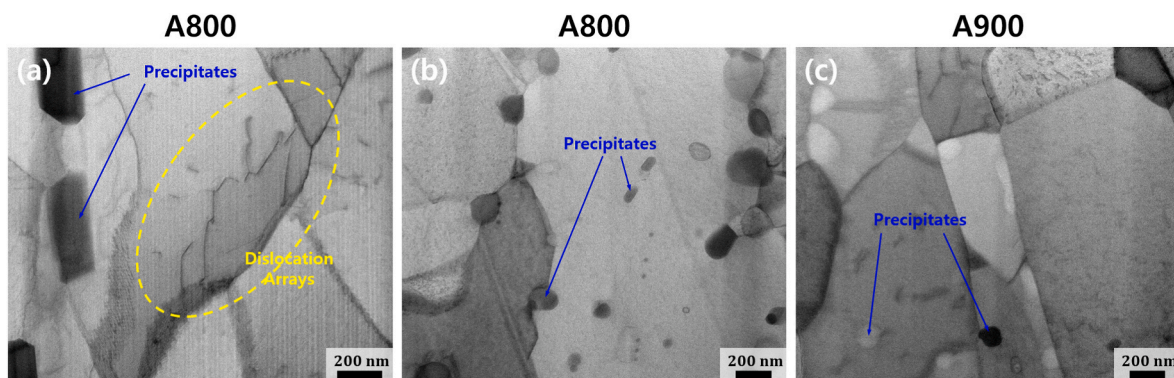

Fig. 4. STEM BF micrographs of **(a)** recovered grains of the A800 sample, **(b)** recrystallized grains of the A800 sample, and **(c)** recrystallized grains of the A900 sample.
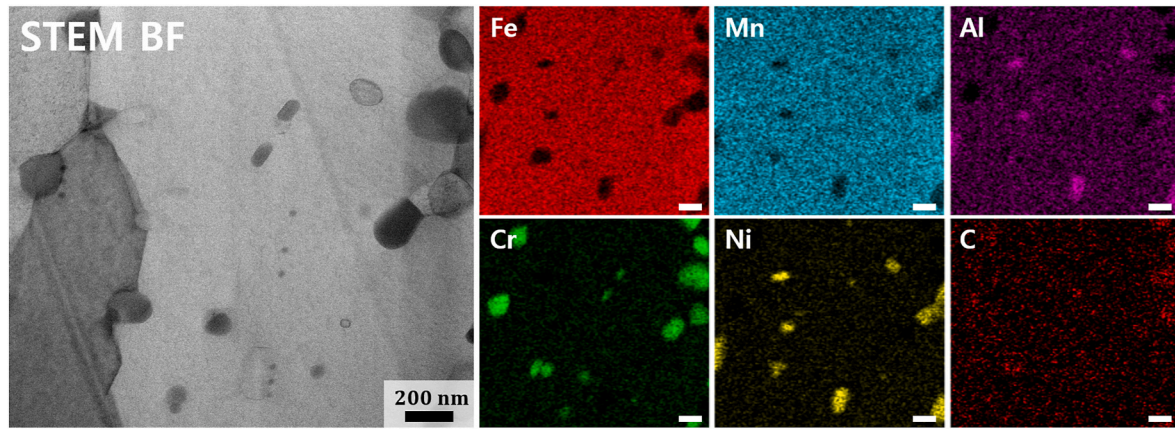
Fig. 5. STEM BF image and TEM-EDS elemental mapping results for a recrystallized region of the A800 sample.

strength even in pre-existing dislocation-free fully recrystallized regions [33,34].

3.3. Tensile properties

Fig. 6 shows the mechanical properties of the A700, A800, and A900 samples, and Table 1 summarizes them: YS, ultimate tensile strength (UTS), uniform elongation (UEL), and total elongation (TEL). The MEA presented a tendency to decrease strength and increase ductility as the annealing heat treatment temperature increased. The A700 sample, which had some cold-rolled microstructure remaining, had the lowest UEL and TEL of 7.15%, but showed the highest strength with the YS of 1241.2 MPa and the UTS of 1524.5 MPa. Considering that the theoretical density of the MEA was determined to be 6.803 g/cm^3, specific YS and specific UTS were 182.4 MPa cm^3/g and 224.1 MPa cm^3/g, respectively. The A800 sample, which consists of recrystallized grains, non-recrystallized grains, and recovered grains, exhibited the most balanced combination of strength and elongation among the three conditions. The A800 sample achieved both the Giga-Pascal YS and UTS while maintaining the UEL of 13.3% and TEL of 18.6%. Its specific YS and specific UTS were calculated to be 147.7 MPa cm^3/g and 192.9 MPa cm^3/g, respectively. The A900 sample had the lowest specific YS and the specific UTS of 114.8 MPa cm^3/g and 168.6 MPa cm^3/g, respectively, but its fully recrystallized microstructure brought excellent ductility with a UEL of 22.1%.

To prove the suitability of the MEA as a lightweight structural material, it was compared with CoCrFeMnNi HEA (as a representative HEA), CoCrNi MEA (as a representative MEA), lightweight HEAs, lightweight Fe–Mn–Al–C steels (as an alloy system with a chemical

Table 1

Summary of mechanical response measured in tensile testing of the $Fe_{47}Mn_{25}Al_{13}Cr_7Ni_5C_3$ MEA.

	YS, MPa	UTS, MPa	UEL, %	TEL, %
A700	1241.2	1524.5	7.15	7.15
A800	1004.9	1312.3	13.3	18.6
A900	781.3	1147.1	22.1	30.9

composition similar to the MEA), and STS 316L (as a representative steel) (Fig. 7) [35–40]. Although we attempted to compare with a larger group of lightweight HEAs/MEAs, it was not possible because most of the developed lightweight HEAs/MEAs were evaluated for their mechanical properties using compressive tests. The CoCrFeMnNi HEA has a high theoretical density of 7.964 g/cm^3, which is 1.161 g/cm^3 heavier than the MEA [41]. Hence, the CoCrFeMnNi HEA ranked lower than alloys developed for lightweight purposes in both the specific YS-UEL combination and the specific UTS-UEL combination [35]. Similarly, the CoCrNi MEA had reasonable strength and elongation, but was inferior in terms of specific YS and specific UTS considering its theoretical density of 8.333 g/cm^3 [36]. The lightweight HEAs had a very low density of 3–4 g/cm^3 with a strategy using aluminum as the principal element and thus they exhibited excellent specific YS and specific UTS. However, they had the characteristics of low ductility and are located on the left side of the Ashby plot [37,38]. The lightweight Fe–Mn–Al–C steels had a similar chemical composition to the MEA, but their YS and UTS were lower than those of the MEA, so they were located at the bottom of the specific YS vs. UEL and specific UTS vs. UEL Ashby plots [39]. The STS 316L is known to have reasonable tensile properties,
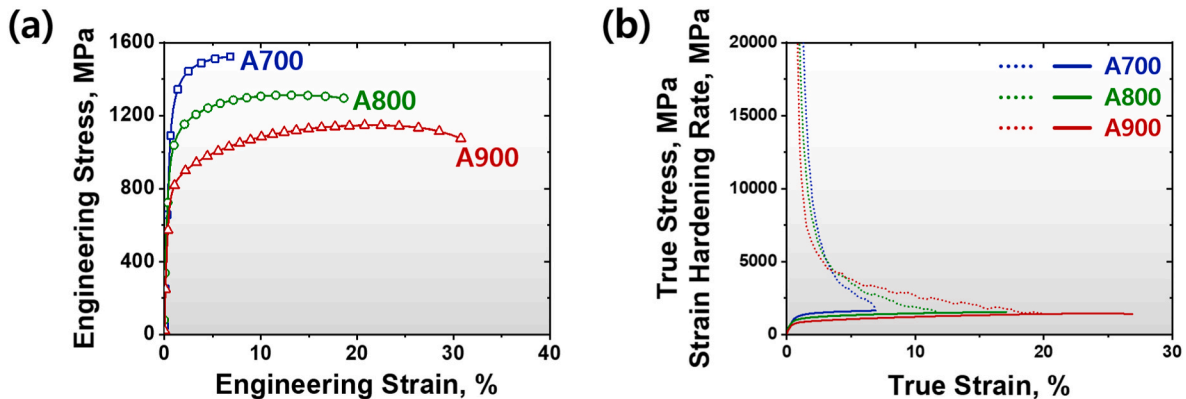

Fig. 6. Tensile properties of the $Fe_{47}Mn_{25}Al_{13}Cr_7Ni_5C_3$ MEA. **(a)** Engineering stress vs. engineering strain curves and **(b)** true stress and strain hardening rate vs. true strain curves.
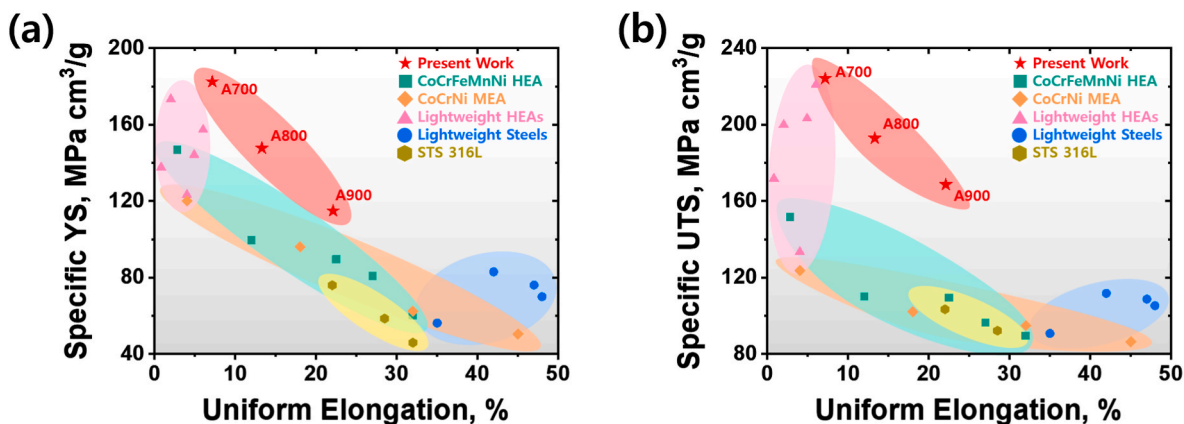
Fig. 7. Ashby plots of **(a)** specific YS vs. UEL and **(b)** specific UTS vs. UEL for comparison of tensile properties of the $Fe_{47}Mn_{25}Al_{13}Cr_7Ni_5C_3$ MEA with CoCrFeMnNi HEA, CoCrNi MEA, lightweight HEAs, lightweight Fe–Mn–Al–C steels, and STS 316L [35–40].

but it had a relatively high density of 8.027 g/cm^3 due to its high iron and nickel contents without low-density alloying elements, resulting in low specific YS and specific UTS [40].

Meanwhile, the MEA brought the benefits of both steel and aluminum alloy with its iron-based design and large amounts of aluminum addition. The chemical composition of the MEA consisted of iron as the principal element, but its proportion was low (47 at%) and the proportion of aluminum was quite high (13 at%), resulting in a density that was 1.071 g/cm^3 lower than the theoretical density of pure iron (7.874 g/cm^3). Therefore, superior specific YS and specific UTS were achieved, surpassing the CoCrFeMnNi HEA and lightweight steel. In addition, since it follows the excellent ductility of iron-based alloy, it exhibited higher ductility compared to the lightweight HEA. For these reasons, the MEA achieved excellent specific YS-UEL and specific UTS-UEL combinations compared to previous lightweight alloy studies.

3.4. Deformation mechanisms

Fig. 8 shows BSE micrographs of the deformed microstructure of the A700, A800, and A900 samples. The magnification of deformed BSE images varied depending on the purpose of observation of each sample. The MEA confirmed that there were only stable phases without metastable phases using thermodynamic calculations (Gibbs free energy for the phase transformation at room temperature was calculated to be −254.7 J/mol) and that no additional twin boundaries were found in the deformed microstructure. Hence, the plastic deformation mechanism of the MEA was mainly due to the generation and accumulation of dislocations [42].

The undeformed A700 sample consisted of a cold-rolled microstructure with a deformed structure and nanometer-sized grains recrystallized along the shear bands (Fig. 3(a)). In the microstructure of the deformed A700 sample, coarse-grains with a deformed structure and

nanometer-sized grains recrystallized within the coarse grains were observed (Fig. 8(a)), identical to its initial state. The A700 sample, in which dislocations were not resolved during the annealing heat treatment, had a high pre-existing dislocation density even in the undeformed state. Such a high pre-existing dislocation density of the A700 sample makes it difficult for dislocations to be further generated and moved when it undergoes tensile plastic deformation. Therefore, not many dislocations were additionally generated during the tensile deformation of the A700 sample, which results in the initial and deformed microstructures being observed similarly. Such specific deformation behavior can also be confirmed in the tensile properties (Fig. 6 and Table 1). The strain hardening rate at the beginning of plastic deformation in the A700 sample was the highest among the three conditions, as larger forces were required due to the inhibition of dislocation generation and movement with high pre-existing dislocation density. However, saturation of dislocations led to early plastic instability and material failure, resulting in lower UEL and TEL of the A700 sample than other samples.

The A800 sample, which consisted of multiple regions, exhibited different deformation behavior in each region. The regions with little microstructural evolution (i.e., prior grains remained as deformed structures and recrystallized nanometer-sized grains along with rolling shear bands) that initially have a deformed structure were limited in the further generation and movement of dislocation during tensile deformation (Fig. 3(b2)). Hence, the grains did not elongate along the loading direction and its dislocation structure did not change significantly despite plastic deformation. The restricted dislocation behavior in this region was the major contributor to the excellent Giga-Pascal strength of the A800 sample (Fig. 6 and Table 1). Meanwhile, the initial microstructures of the recovered grain regions and recrystallized grain regions showed almost no remaining dislocations attributed to annihilation and rearrangement mechanisms and nucleation and grain growth
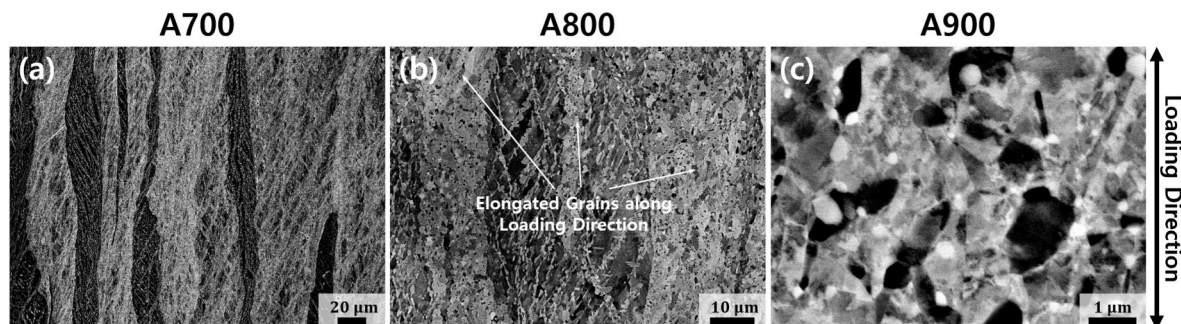

Fig. 8. BSE micrographs observing deformed microstructures of the **(a)** A700, **(b)** A800, and **(c)** A900 samples.

mechanisms, respectively (Fig. 3(b2) and (b3)) and Fig. 4(a) and (b)). These regions were plastically deformable under tensile loading conditions because they had low pre-existing dislocation densities and thus dislocations could be freely generated and moved. The recovered and recrystallized grains observed in the initial microstructure had an equiaxed fine grain structure (Fig. 3(b2)), but were elongated along the tensile loading direction after undergoing tensile plastic deformation (Fig. 8(b)). It allows for a reasonable ductility to the A800 sample, so collaboration with prior grains with high-strength characteristics achieved an excellent strength-ductility combination.

The deformed A900 sample showed a typical deformed microstructure with entangled dislocations (Fig. 8(c)). The A900 sample was fully recrystallized, so its strength and strain hardening rate at the beginning of plastic deformation were lower than those of the other two samples. Conversely, the microstructure consisting only of plastically deformable regions led to excellent ductility of the A900 sample. In the plastic deformation of typical metallic materials, dislocations are generated and accumulated during plastic deformation, affecting flow stress as increasingly larger forces are required due to their strain-hardening nature. Here, the A900 sample can effectively hinder dislocation movements primarily attributed to the grain boundaries of ultrafine grains and randomly distributed $M_{23}C_6$ and B2 precipitates. Therefore, the A900 sample was able to obtain reasonable strength while maintaining excellent ductility with fully recrystallized microstructures.

4. Conclusions

In conclusion, we designed a lightweight MEA that simultaneously satisfies low density and excellent mechanical properties. Three types of samples, A700, A800, and A900, were prepared under different annealing heat treatment conditions, and the following conclusions were derived.

(i) The MEA under the annealing heat treatment conditions performed in this study was all composed of $M_{23}C_6$ and B2 precipitates in an FCC matrix, but the degree of microstructural evolution was different. The A700 and A800 samples showed partially recrystallized microstructures, and the A900 sample had a fully recrystallized microstructure.

(ii) Due to the insufficient microstructural evolution driving force, the A700 sample showed a cold-rolled microstructure of a deformed structure elongated along the RD and nanometer-sized grains recrystallized along the shear bands. The microstructure with high pre-existing dislocation density effectively prevented further generation and movement of dislocations, boasting the high specific YS (182.4 MPa cm^3/g) and specific UTS (224.1 MPa cm^3/g). However, saturated dislocations led to early plastic instability and material failure, resulting in a relatively low UEL of 7.15%.

(iii) The microstructure of the A800 sample consisted of various regions: the deformed coarse-grain region with nanometer-sized grains recrystallized, the recrystallized ultrafine-grain region, and the recovered grain region. The synergistic effect of the high strength of the regions remaining as a deformed structure and the high ductility of the dislocation-free regions enabled an excellent strength-elongation combination of Giga-Pascal level strength and the UEL of 13.3% for the A800 sample.

(iv) With sufficient microstructural evolution driving force, the A900 sample had ultrafine-grained fully recrystallized microstructures. Although there were no deformed regions in the initial microstructure, the grain boundaries of ultrafine grains and randomly distributed $M_{23}C_6$ and B2 precipitates effectively hindered the movement of dislocations, resulting in the A900 sample having reasonable strength. Moreover, the microstructure consisting

only of plastically deformable recrystallized regions brought excellent UEL of 22.1%.

(v) The designed MEA showed superior specific YS-UEL and specific UTS-UEL combinations compared to previously studied lightweight HEAs and steel. The lightweight, inexpensive, strong, and ductile MEA and its design strategy will make a significant contribution to the automotive industry in terms of crash resistance and fuel efficiency. In the next study, we plan to investigate the corrosion resistance as an advantage of manganese among the elements added to the MEA.

CRediT authorship contribution statement

Gang Hee Gu: Conceptualization, Data curation, Formal analysis, Investigation, Methodology, Visualization, Writing – original draft. **Hyeonseok Kwon:** Conceptualization, Data curation, Formal analysis, Investigation, Methodology, Visualization, Writing – review & editing. **Jae Heung Lee:** Data curation, Formal analysis, Investigation, Methodology. **Takayoshi Nakano:** Formal analysis, Investigation, Methodology. **Hyoung Seop Kim:** Conceptualization, Funding acquisition, Project administration, Resources, Supervision, Validation, Writing – review & editing.

Declaration of competing interest

The authors declare that they have no known competing financial interests or personal relationships that could have appeared to influence the work reported in this paper.

Data availability

Data will be made available on request.

Acknowledgments

References

[1] C.-Y. Hsu, J.-W. Yeh, S.-K. Chen, T.-T. Shun, Wear resistance and high-temperature compression strength of fcc CuCoNiCrAl$_{0.5}$Fe alloy with boron addition, Metall. Mater. Trans. A 35 (2004) 1465–1469, https://doi.org/10.1007/s11661-004-0254-x.

[2] K.-K. Wong, H.-C. Hsu, S.-C. Wu, W.-F. Ho, Novel metastable nonequiatomic Ti-Zr-Nb-Mo medium entropy alloys with high yield strength-to-elastic-modulus ratios, Met. Mater. Int. 28 (2022) 2563–2570, https://doi.org/10.1007/s12540-021-01122-3.

[3] B. Cantor, I.T.H. Chang, P. Knight, A.J.B. Vincent, Microstructural development in equiatomic multicomponent alloys, Mater. Sci. Eng., A 375–377 (2004) 213–218, https://doi.org/10.1016/j.msea.2003.10.257.

[4] J.-W. Yeh, S.-K. Chen, S.-J. Lin, J.-Y. Gan, T.-S. Chin, T.-T. Shun, C.-H. Tsau, S.-Y. Chang, Nanostructured high-entropy alloys with multiple principal elements: novel alloy design concepts and outcomes, Adv. Eng. Mater. 6 (2004) 299–303, https://doi.org/10.1002/adem.200300567.

[5] J.-W. Yeh, Recent progress in high entropy alloys, Ann. Chim. Sci. Mater. 31 (2006) 633–648.

[6] J. Kumar, A. Linda, M. Sadhasivam, K.G. Pradeep, N.P. Gurao, K. Biswas, The effect of Al addition on solid solution strengthening in CoCrFeMnNi: experiment and modelling, Acta Mater. 238 (2022), 118208, https://doi.org/10.1016/j.actamat.2022.118208.

[7] J.G. Kim, J.W. Bae, J.M. Park, W. Woo, S. Harjo, S. Lee, H.S. Kim, Effect of the difference in strength of hard and soft components on the synergetic strengthening of layered materials, Met. Mater. Int. 27 (2021) 376–383, https://doi.org/10.1007/s12540-020-00657-1.

[8]   J. Li, K.G. Pradeep, Y. Deng, D. Raabe, C.C. Tasan, Metastable high-entropy dual-phase alloys overcome the strength–ductility trade-off, Nature 534 (2016) 227–230, https://doi.org/10.1038/nature17981.

[9]   Z. Li, C.C. Tasan, K.G. Pradeep, D. Raabe, A TRIP-assisted dual-phase high-entropy alloy: grain size and phase fraction effects on deformation behavior, Acta Mater. 131 (2017) 323–325, https://doi.org/10.1016/j.actamat.2017.03.069.

[10]   H. Kwon, P. Sathiyamoorthi, M.K. Gangaraju, A. Zargaran, J. Wang, Y.-U. Heo, S. Harjo, W. Gong, B.-J. Lee, H.S. Kim, High-density nanoprecipitates and phase reversion via maraging enable ultrastrong yet strain-hardenable medium-entropy alloy, Acta Mater. 248 (2023), 118810, https://doi.org/10.1016/j.actamat.2023.118810.

[11]   Z. Li, Interstitial equiatomic CoCrFeMnNi high-entropy alloys: carbon content, microstructure, and compositional homogeneity effects on deformation behavior, Acta Mater. 164 (2019) 400–412, https://doi.org/10.1016/j.actamat.2018.10.050.

[12]   L. Xia, Q. Wu, K. Zhou, B. Han, F. He, Z. Wang, Concurrent recrystallization and precipitation for combination of superior precipitation and grain boundary hardening in $Co_{37}Cr_{20}Ni_{37}Ti_3Al_3$ High-Entropy Alloy, Met. Mater. Int. 28 (2022) 2863–2873, https://doi.org/10.1007/s12540-022-01178-9.

[13]   Y.C. Liao, T.H. Li, P.H. Tsai, J.S.C. Jang, K.C. Hsieh, C.Y. Chen, J.C. Huang, H.J. Wu, Y.C. Lo, C.W. Huang, I.Y. Tsao, Designing novel lightweight, high-strength and high-plasticity Tix(AlCrNb)100-x medium-entropy alloys, Intermetallics 117 (2020), 106673, https://doi.org/10.1016/j.intermet.2019.106673.

[14]   L.C. Liao, P.S. Chen, P.H. Tsai, J.S.C. Jang, K.C. Hsieh, H.W. Chang, C.Y. Chen, J.C. Huang, H.J. Wu, Y.C. Lo, C.W. Huang, I.Y. Tsao, Effect of thermomechanical treatment on the microstructure evolution and mechanical properties of lightweight Ti65(AlCrNb)35 medium-entropy alloy, Intermetallics 143 (2022), 107470, https://doi.org/10.1016/j.intermet.2022.107470.

[15]   M. Wang, Y. Lu, J. Lan, T. Wang, C. Zhang, Z. Cao, T. Li, P.K. Liaw, Lightweight, ultrastrong and high thermal-stable eutectic high-entropy alloys for elevated-temperature applications, Acta Mater. 248 (2023), 118806, https://doi.org/10.1016/j.actamat.2023.118806.

[16]   S. Chen, R. Rang, A. Haldar, R.K. Ray, Current state of Fe-Mn-Al-C low density steels, Prog. Mater. Sci. 89 (2017) 345–391, https://doi.org/10.1016/j.pmatsci.2017.05.002.

[17]   J.-K. Ren, L. Zhang, Z.-H. Li, J. Chen, W.-N. Zhang, S.-W. Wu, Z.-Y. Liu, Fe-Mn-Al-C high-entropy steels with superior mechanical properties at 4.2 K, Mater. Des. 228 (2023), 111840, https://doi.org/10.1016/j.matdes.2023.111840.

[18]   J.-O. Andersson, T. Helander, L. Höglund, P. Shi, B. Sundman, Thermo-Calc & DICTRA, computational tools for materials science, Calphad 26 (2002) 273–312, https://doi.org/10.1016/S0364-5916(02)00037-8.

[19]   G.H. Gu, H. Kwon, Y. Kim, F. Haftlang, Y.-U. Heo, H.S. Kim, Unprecedented bake hardening responses of interstitial high-entropy alloy by synergistic effect with lattice distortion, Mater. Des. 233 (2023), 112289, https://doi.org/10.1016/j.matdes.2023.112289.

[20]   K. Li, Z. Jiao, Y. Bai, Z. Li, Z. Wang, Cooperative strengthening effect of transformation-induced plasticity and twinning-induced plasticity on strain hardening in a novel metallic glass matrix composite subjected to dynamic compression, Mater. Sci. Eng., A 840 (2022), 142987, https://doi.org/10.1016/j.msea.2022.142987.

[21]   G.H. Gu, R.E. Kim, J. Lee, H.S. Kim, Tailoring microstructure with spatial heterogeneity in CoCrFeMnNi high-entropy alloy via laser surface relaxation, Mater. Sci. Eng., A 852 (2022), 143720, https://doi.org/10.1016/j.msea.2022.143720.

[22]   J.P. Oliveira, T.M. Curado, Z. Zeng, J.G. Lopes, E. Rossinyol, J.M. Park, N. Schell, F.M. Braz Fernandes, H.S. Kim, Gas tungsten arc welding of as-rolled CrMnFeCoNi high entropy alloy, Mater. Des. 189 (2020), 108505, https://doi.org/10.1016/j.matdes.2020.108505.

[23]   R. Li, L. Xie, W.Y. Wang, P.K. Liaw, Y. Zhang, High-throughput calculations for high-entropy alloys: a review, Front. Mater. 7 (2020) 290, https://doi.org/10.3389/fmats.2020.00290.

[24]   L. Jia, X. Ren, H. Hou, Y. Zhang, Microstructural evolution and superplastic deformation mechanisms of as-rolled 2A97 alloy at low-temperature, Mater. Sci. Eng., A 759 (2019) 19–29, https://doi.org/10.1016/j.msea.2019.04.102.

[25]   X. Cui, Y. Yang, Y. Zhu, M. Li, C. Wen, B. Jiang, X. Peng, F. Pan, Synergetic regulation of microstructure, mechanical properties and corrosion resistance of as-rolled Mg–3Y alloy by annealing treatment, J. Mater. Res. Technol. 22 (2023) 683–695, https://doi.org/10.1016/j.jmrt.2022.11.114.

[26]   H. Kwon, A. Zargaran, P. Ashghri-Rad, E.S. Kim, G.H. Gu, J. Lee, J. Moon, J.W. Bae, H.S. Kim, Metastability engineering of partially recrystallized C-doped non-equiatomic CoCrFeNiMo medium-entropy alloy, Appl. Phys. Lett. 119 (2021), 141901, https://doi.org/10.1063/5.0065000.

[27]   G. Li, S. Lyu, R. Zheng, M. Kawabata, C. Ma, Q. Li, K. Ameyama, Further optimization of strength and ductility in a harmonic structure designed pure copper via thermomechanical processing, Mater. Sci. Eng., A 790 (2020), 139687, https://doi.org/10.1016/j.msea.2020.1396870.

[28]   C. Zheng, Y. Wang, J. Jin, P. Gong, X. Wang, H. Wen, M. Zhang, Recrystallization and grain growth behavior of variously deformed CoCrFeMnNi high-entropy alloys: microstructure characterization and modeling, J. Mater. Res. Technol. 20 (2022) 2277–2292, https://doi.org/10.1016/j.jmrt.2022.07.182.

[29]   P. Wang, J. Chen, B. Sun, D. Zhu, Y. Cao, Effects of annealing process parameters on microstructural evolution and strength-ductility combination of CoCrFeMnNi high-entropy alloy, Mater. Sci. Eng., A 840 (2022), 142880, https://doi.org/10.1016/j.msea.2022.142880.

[30]   P. Sathiyamoorthi, P. Asghari-Rad, J.W. Bae, H.S. Kim, Fine tuning of tensile properties in CrCoNi medium entropy alloy through cold rolling and annealing, Intermetallics 113 (2019), 106578, https://doi.org/10.1016/j.intermet.2019.106578.

[31]   Z. Li, Interstitial equiatomic CoCrFeMnNi high-entropy alloys: carbon content, microstructure, and compositional homogeneity effects on deformation behavior, Acta Mater. 164 (2019) 400–412, https://doi.org/10.1016/j.actamat.2018.10.050.

[32]   G.W. Hu, L.C. Zeng, H. Du, Q. Wang, Z.T. Fan, X.W. Liu, Combined effects of solute drag and Zener pinning on grain growth of a NiCoCr medium-entropy alloy, Intermetallics 136 (2021), 107271, https://doi.org/10.1016/j.intermet.2021.107271.

[33]   X. Gao, Y. Lu, B. Zhang, N. Liang, G. Wu, G. Sha, J. Liu, Y. Zhao, Microstructural origins of high strength and high ductility in an AlCoCrFeNi2.1 eutectic high-entropy alloy, Acta Mater. 141 (2017) 59–66, https://doi.org/10.1016/j.actamat.2017.07.041.

[34]   J. Hidalgo, M. Vittorietti, H. Farahani, F. Vercruysse, R. Petrov, J. Sietsma, Influence of $M_{23}C_6$ carbides on the heterogeneous strain development in annealed 420 stainless steel, Acta Mater. 200 (2020) 74–90, https://doi.org/10.1016/j.actamat.2020.08.072.

[35]   P. Wang, J. Chen, B. Sun, D. Zhu, Y. Cao, Effects of annealing process parameters on microstructural evolution and strength-ductility combination of CoCrFeMnNi high-entropy alloy, Mater. Sci. Eng., A 840 (2022), 142880, https://doi.org/10.1016/j.msea.2022.142880.

[36]   S. Yoshida, T. Bhattacharjee, Y. Bai, N. Tsuji, Friction stress and Hall-Petch relationship in CoCrNi equi-atomic medium entropy alloy processed by severe plastic deformation and subsequent annealing, Scripta Mater. 134 (2017) 33–36, https://doi.org/10.1016/j.scriptamat.2017.02.042.

[37]   Y. Xie, X. Meng, R. Zang, Y. Chang, L. Wan, Y. Huang, Deformation-driven modification towards strength-ductility enhancement in Al–Li–Mg–Zn–Cu lightweight high-entropy alloys, Mater. Sci. Eng., A 830 (2022), 142332, https://doi.org/10.1016/j.msea.2021.142332.

[38]   R. Li, Z. Ren, Y. Wu, Z. He, P.K. Liaw, J. Ren, Y. Zhang, Mechanical behaviors and precipitation transformation of the lightweight high-Zn-content Al–Zn–Li–Mg–Cu alloy, Mater. Sci. Eng., A 802 (2021), 140637, https://doi.org/10.1016/j.msea.2020.140637.

[39]   C.-Y. Lee, J. Jeong, J. Han, S.-J. Lee, S. Lee, Y.-K. Lee, Coupled strengthening in a medium manganese lightweight steel with an inhomogeneously grained structure of austenite, Acta Mater. 84 (2015) 1–8, https://doi.org/10.1016/j.actamat.2014.10.032.

[40]   W. Qin, J. Li, Y. Liu, J. Kang, L. Zhu, D. Shu, P. Peng, D. She, D. Meng, Y. Li, Effects of grain size on tensile property and fracture morphology of 316L stainless steel, Mater. Lett. 254 (2019) 116–119, https://doi.org/10.1016/j.matlet.2019.07.058.

[41]   M.A. Gianelle, C. Clapp, A. Kundu, H.M. Chan, Solid state processing of the cantor derived alloy CoCrFeMnNi by oxide reduction, Results Mater 14 (2022), 100286, https://doi.org/10.1016/j.rinma.2022.100286.

[42]   R. Young, J. Fuller-Thomson, H. Zurob, O. Bouaziz, A. Arlazarov, Assessment of phase transformations in binary Fe-Mn alloys: effects of composition and of plastic strain, Met. Mater. Int. 28 (2022) 1537–1548, https://doi.org/10.1007/s12540-021-01043-1.